Draft version June 28, 2022
Typeset using LaTeX default style in AASTeX631

Confinement of the Solar Tachocline by Dynamo Action in the Radiative Interior

Loren I. Matilsky,[1] Bradley W. Hindman,[2,1] Nicholas A. Featherstone,[3] Catherine C. Blume,[1] and Juri Toomre[1]

[1] *JILA & Department of Astrophysical and Planetary Sciences, University of Colorado Boulder, Boulder, CO 80309-0440, USA*
[2] *Department of Applied Mathematics, University of Colorado Boulder, Boulder, CO 80309-0526, USA*
[3] *Southwest Research Institute, 1050 Walnut Street Suite 400, Boulder, CO 80302, USA*

Submitted to ApJL

ABSTRACT

A major outstanding problem in solar physics is the confinement of the solar tachocline, the thin shear layer that separates nearly solid-body rotation in the radiative interior from strong differential rotation in the convection zone. Here, we present the first 3-D, global solar simulation in which a tachocline is confined by a self-excited dynamo. The non-axisymmetric magnetism is initially built in the convection zone and then diffusively imprints downward. Additionally, the field is locally amplified throughout the radiative interior by vigorous horizontal motions that arise from equatorial Rossby waves and possibly shear instabilities. Our work thus challenges the long-held notion that the Sun's dynamo magnetic field is amplified only as deep as the tachocline and stored in a quiescent radiative interior.

Keywords: Solar dynamo; Solar differential rotation; Solar interior; Solar radiative zone; Solar convective zone

1. INTRODUCTION

In the solar tachocline at the base of the convection zone, strong differential rotation (∼30% faster at the equator than at the poles) transitions to nearly solid-body rotation in the radiative interior (e.g., Brown et al. 1989; Howe et al. 2000). Helioseismic estimates of the tachocline's width lie around $0.05R_\odot$, where $R_\odot \equiv 6.96 \times 10^8$ m is the solar radius (Howe 2009). Because of this strong shear, the tachocline likely plays a central role in the solar dynamo. The "interface" dynamo paradigm, in particular, holds that toroidal magnetism is primarily generated by the tachocline's shear (e.g., Parker 1993; Charbonneau & MacGregor 1997), and is then stored for long time intervals in the quiescent radiative interior (e.g., Spruit & van Ballegooijen 1982; Parker 1993; Ferriz-Mas & Schuessler 1994).

Without an opposing mechanism, inward radiative diffusion of latitudinal temperature gradients from the convection zone is expected to drive meridional circulations in the stable layer that would have imprinted differential rotation deep into the interior by the current age of the Sun (Spiegel & Zahn 1992). To achieve a thin tachocline, the Sun must have a torque that forces solid-body rotation in the radiative interior and thus counters radiative spread. Several prevalent tachocline confinement scenarios postulate the origin of this torque. In the "fast hydrodynamic (HD) scenario" (Spiegel & Zahn 1992), the torque is caused by the Reynolds stresses associated with primarily HD instabilities of the horizontal flows and is generated on the timescale of months to years. In the "slow magnetohydrodynamic (MHD) scenario" (Gough & McIntyre 1998), the torque is due to a primordial magnetic field and is generated on the timescale of radiative spread, namely, $\sim 10^{11}$ years. Finally, in the "fast MHD scenario," the torque comes from the cyclic dynamo magnetic field in the convection zone imprinting diffusively downward to a skin depth, similar to the skin effect for AC currents in a conductor (Forgács-Dajka & Petrovay 2001).

Corresponding author: Loren I. Matilsky
loren.matilsky@colorado.edu

Many theoretical studies have characterized the instabilities believed to cause a fast HD scenario (e.g., Charbonneau et al. 1999a; Gilman & Dikpati 2014; Garaud 2020) and have examined how an assumed primordial or cycling magnetic field might cause a slow or fast MHD scenario (e.g., Garaud 2002; Acevedo-Arreguin et al. 2013; Barnabé et al. 2017; Wood & Brummell 2018). For global, 3-D simulations, computationally tractable values of the thermal Prandtl number and buoyancy frequency do not permit substantial radiative spread (e.g., Acevedo-Arreguin et al. 2013; Wood & Brummell 2012); instead, the tachocline spreads viscously. Transient tachoclines have been included in prior global dynamo simulations by implementing a very small viscosity below the convection zone (e.g., Brun et al. 2011; Guerrero et al. 2016). The tachocline still spreads inward slowly, but for the timescale on which the simulation is run, it is effectively stationary and its influence on the dynamo can be assessed.

Here, we present two 3-D, global, nonlinear simulations of a rotating solar-like star—an HD case and an MHD case—that include a radiative interior coupled to an outer convection zone. In the HD case, the differential rotation viscously imprints throughout the entire radiative interior. In the MHD case, by contrast, dynamo action creates a cycling, non-axisymmetric magnetic field whose torque enforces solid-body rotation in the radiative interior and maintains a statistically steady tachocline. The magnetism in the radiative interior arises both from diffusive imprinting of field from the overlying convection zone (similar to the fast MHD confinement scenario), and also from local inductive amplification. This dynamo action occurs even below the convective overshoot layer and arises from strong horizontal motions due to equatorially confined (equatorial) Rossby waves (Gizon et al. 2020) and possibly shear instabilities as well.

2. NUMERICAL EXPERIMENT

We use the Rayleigh code (Featherstone & Hindman 2016; Matsui et al. 2016; Featherstone et al. 2021) to evolve the anelastic fluid equations (e.g., Gilman & Glatzmaier 1981) in a rotating spherical shell that spans $r_{\rm min} = 0.491 R_\odot$ to $r_{\rm max} = 0.947 R_\odot$. We use spherical coordinates: r (radius), θ (colatitude), and ϕ (azimuth angle). The background stellar structure is hydrostatic, spherically symmetric, and time-independent. The background entropy gradient enforces strong convective stability in the radiative interior and weak convective instability in the convection zone. The transition between stability and instability nominally occurs at $r_0 \equiv 0.719 R_\odot$. More details on the thermodynamic state are given in Appendix A.

Our shell covers approximately equal thickness in both the convection zone and radiative interior, corresponding to the top ∼2.1 density scale heights of the Sun's radiative interior and the bottom 3 density scale heights of the convection zone. Our grid resolution is $N_\theta = 384$ and $N_\phi = 768$ in the horizontal directions (the maximum spherical-harmonic degree after dealiasing is $\ell_{\rm max} = 255$). We use three stacked Chebyshev domains in the vertical direction (each with 64 grid points) with boundaries at $(0.491, 0.669, 0.719, 0.947) R_\odot$. The two internal boundaries maximize grid resolution at the transition from stability to instability.

As in Matilsky & Toomre (2020a, 2021), we rotate at three times the solar Carrington rate ($\Omega_0 = 3\Omega_\odot$, where $\Omega_\odot = 2.87 \times 10^{-6}$ rad s^{-1}; $\Omega_\odot/2\pi = 457$ nHz; $2\pi/\Omega_\odot = 25.4$ days). Rotating faster than the Sun is required to avoid the "anti-solar" states associated with the simulations' overestimating of the fluctuating velocities at large scales (e.g., O'Mara et al. 2016). The frame rotation frequency is $\Omega_0/2\pi = 1370$ nHz and the frame rotation period is $P_{\rm rot} \equiv 2\pi/\Omega_0 = 8.45$ days. A solar luminosity $L_\odot \equiv 3.85 \times 10^{33}$ erg s^{-1} is driven through the convection zone via a fixed internal-heating profile and is removed at the outer boundary via thermal conduction.

At the top of the domain, $\nu(r) = \kappa(r) = 5.00 \times 10^{12}$ cm^2 s^{-1} and $\eta(r) = 1.25 \times 10^{12}$ cm^2 s^{-1}, where $\nu(r)$, $\kappa(r)$, and $\eta(r)$ are the momentum, thermal, and magnetic diffusivities, respectively. All diffusivity profiles increase with radius like $\overline{\rho}(r)^{-1/2}$, where $\overline{\rho}(r)$ is the background density. At both boundaries, we use stress-free and impenetrable conditions on the velocity, potential-field-matching conditions on the magnetic fields, and fixed-conductive-flux conditions (e.g., Matilsky et al. 2020; Anders et al. 2020) on the entropy.

The convection is initialized by weakly perturbing the thermal field randomly throughout the entire shell. The MHD case is additionally initialized by weakly perturbing the magnetic field randomly throughout the convection zone only. We define the HD case's "equilibrated state" as the time interval during which the kinetic energy in the radiative interior is statistically steady. For the MHD case's equilibrated state, we additionally require that the magnetic energy in the radiative interior is statistically steady. We define the viscous and magnetic diffusion times across the radiative interior to be $[r_0 - r_{\rm min}]^2/\nu_0 = 295\ P_{\rm rot}$ and $[r_0 - r_{\rm min}]^2/\eta_0 = 1180\ P_{\rm rot}$, respectively, where the "0" subscript indicates the value of the diffusivity at r_0. The HD case was run in its equilibrated state for 7810 $P_{\rm rot}$ (26.5 viscous diffusion times) and the MHD case for 12500 $P_{\rm rot}$ (10.6 magnetic diffusion times).

The convection zone (defined to be the region where the convective heat transport is positive) has a base $r_{\rm bcz}$ that is set by the balance of radial energy fluxes in equilibrium. Convective downflows overshoot into a thin layer within the stable region, the top of which is $r_{\rm bcz}$ and the base of which is $r_{\rm ov}$ (defined to be the location below which there is negligible convective heat transport). For the MHD case, $r_{\rm bcz} = 0.729 R_\odot$ and $r_{\rm ov} = 0.710 R_\odot$. We define the radiative interior as the layer spanning $r_{\rm min}$ to $r_{\rm ov}$. Calculation of $r_{\rm ov}$ and $r_{\rm bcz}$ for each case is done explicitly in Appendix A. The non-dimensional parameters characterizing each case are given in Appendix B.

3. STEADY-STATE SOLID-BODY ROTATION IN THE RADIATIVE INTERIOR

We define the rotation rate as $\Omega(r,\theta) \equiv \Omega_0 + \langle v_\phi \rangle_{\rm t} / r\sin\theta$ and the rotation frequency as $\Omega/2\pi$, where v_ϕ is the azimuthal velocity. Throughout the text, angular brackets with no subscript denote a zonal average at a particular instant, whereas a "t" subscript denotes a combined temporal and zonal average, and a "sph" subscript denotes a combined temporal and spherical-surface average. Unless otherwise specified, temporal averages are taken over the full equilibrated state. Figures 1(a, b) show the equilibrated rotation-frequency profiles for both simulations in the meridional plane. In the HD case, the differential rotation has viscously imprinted throughout the entire radiative interior. In the MHD case, however, the radiative interior has nearly solid-body rotation.

Figure 1(c) shows the rotation profile in the MHD case as a function of radius for various latitudes. We define the radially varying latitudinal rotation contrast $\Delta\Omega(r)$ as the difference in rotation rate between the equator and 60° latitude at a fixed radius. In the HD case, $\Delta\Omega(r)/\Omega_0 \sim 0.2$ throughout the whole shell. The MHD case has $\Delta\Omega(r)/\Omega_0 = 4.2\times10^{-2} \equiv \Delta\Omega_{CZ}/\Omega_0$ at the top of the convection zone and $\Delta\Omega(r)/\Omega_0 = 7.6\times10^{-4} \equiv \Delta\Omega_{RI}/\Omega_0$ at the bottom of the radiative interior. We define the base of the tachocline, $r_{\rm tach} = 0.641 R_\odot$, to be the radial location where $\Delta\Omega(r)$ has dropped by a factor of 20 from its value at the top of the convection zone and call the layer spanning $r_{\rm tach}$ to $r_{\rm bcz}$ the MHD case's tachocline.

The velocity and magnetic-field amplitudes for the MHD case are shown in Figures 1(d, e). Below the overshoot layer, the vertical components of the fluctuating velocity, $\boldsymbol{v'} \equiv \boldsymbol{v} - \langle \boldsymbol{v} \rangle$, and fluctuating magnetic field, $\boldsymbol{B'} \equiv \boldsymbol{B} - \langle \boldsymbol{B} \rangle$, are small compared to the horizontal components. Due to the stable stratification, v_r' falls by ∼2 orders of magnitude over the overshoot layer and by ∼5 orders of magnitude over the whole radiative interior.

The non-axisymmetric magnetic field in the MHD case is composed mainly of azimuthal orders $m = 1$ and $m = 2$. Figures 2(a–d) show snapshots of the horizontal field components B_ϕ and B_θ at two different depths. At both depths, the same large-scale structure is apparent in each field component, though it is significantly smoother and more coherent in the deeper layer. The topology is similar to the "partial wreaths" we identified in convection-zone only dynamo simulations (Matilsky & Toomre 2020a,b). In that work, an initially regularly cycling dynamo composed of full magnetic wreaths (strong $m = 0$ signature) destabilized into two partial wreaths (strong $m = 1$ signature). The partial wreaths were essentially stationary in a properly chosen rotating frame and reversed their polarity (sign of the $m = 0$ component) through in-place amplitude modulation. The polarity-reversal time varied, forming a quasi-cyclic dynamo with multiple frequency components.

Figure 2 shows the real part of the $m = 1$ component of B_θ (two partial wreaths) as a function of time and radius. The partial wreaths appear first in the convection zone and then move downward into the overshoot layer, where they are significantly amplified, before finally penetrating deep into the radiative interior. The other field components (B_r and B_ϕ) also behave this way, as do the $m = 2$ structures. From Figure 2(e), one quasi-regular dynamo cycle occurs every $P_{\rm dyn} \sim 500\ P_{\rm rot}$. Furthermore, the partial wreaths migrate downward at approximately the same speed predicted by the skin effect, namely $v_{\rm skin} \equiv \sqrt{2\eta_{\rm ov}\omega_{\rm dyn}}$, where $\omega_{\rm dyn}/2\pi \equiv 1/P_{\rm dyn} = 2.74$ nHz and $\eta_{\rm ov}$ is the value of the magnetic diffusivity at $r_{\rm ov}$. The skin depth is $\delta_{\rm skin} \equiv \sqrt{2\eta_{\rm ov}/\omega_{\rm dyn}} = 0.082 R_\odot$, which allows the transport of field significantly below the overshoot layer.

4. DYNAMICAL MAINTENANCE OF SOLID-BODY ROTATION

The MHD case's tachocline is statistically steady, wandering by no more than ∼3 nHz from the profile shown in Figures 1(b,c) throughout the equilibrated state. There is thus good temporally averaged torque balance, which we find is primarily between the viscous and magnetic torques:

$$\underbrace{\nabla\cdot\left[\overline{\rho}\nu r^2\sin^2\theta\nabla\Omega\right]}_{\text{viscous torque}\ \equiv\ \tau_{\rm visc}} + \underbrace{\frac{1}{4\pi}\nabla\cdot\left[r\sin\theta\left\langle B_\phi \boldsymbol{B}_{\rm pol}\right\rangle_{\rm t}\right]}_{\text{magnetic torque}\ \equiv\ \tau_{\rm mag}} \approx 0, \tag{1}$$

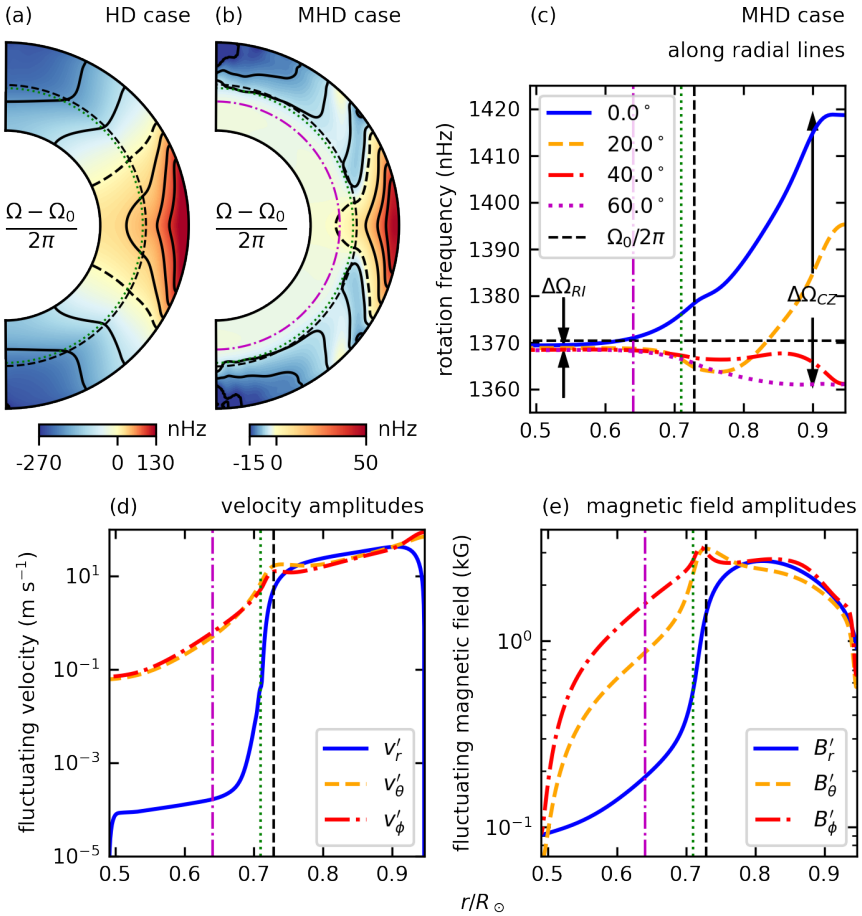

Figure 1. Radiative interior forced into solid-body rotation. (a) Contours of isorotation, $(\Omega - \Omega_0)/2\pi$ = constant, in the HD case, plotted in the meridional plane. Negative values are normalized separately from positive values. There are three equally-spaced positive and negative contours each (solid contours). The zero contour $\Omega = \Omega_0$ is dashed. (b) Like (a), but for the MHD case. (c) Rotation frequency $\Omega/2\pi$ at various latitudes along radial lines in the MHD case. The rotation contrasts in the convection zone and radiative interior are marked by vertical arrows; the frame rotation frequency is marked by the horizontal dashed line. (d) Fluctuating velocity amplitude $\langle|\boldsymbol{v}'|^2\rangle^{1/2}_{\rm sph}$. Each component v'_r, v'_θ, and v'_ϕ is plotted separately. (e) Same as (d), but for $\langle|\boldsymbol{B}'|^2\rangle^{1/2}_{\rm sph}$. In this figure and those that follow, the dashed black, dotted green, and dash-dotted magenta curves refer to $r_{\rm bcz}$, $r_{\rm ov}$, and $r_{\rm tach}$, respectively.

where $\boldsymbol{B}_{\rm pol} \equiv B_r\hat{\boldsymbol{e}}_r + B_\theta\hat{\boldsymbol{e}}_\theta$. Because the dynamo is non-axisymmetric and cycling, we decompose $\boldsymbol{B}$ into its constituent m and frequency ω components $\boldsymbol{B}_{m\omega}$. Each component defines a Fourier mode $\exp(im\phi - i\omega t)$, moving in azimuth angle with phase velocity ω/m. We define the magnetic torque $\tau_{{\rm mag},m\omega}$ from a given $\boldsymbol{B}_{m\omega}$ such that Parceval's theorem can be written $\sum_m\sum_\omega |\boldsymbol{B}_{m\omega}|^2 = \langle|\boldsymbol{B}|^2\rangle_{\rm t}$. Then

$$\tau_{{\rm mag},m\omega} \equiv \frac{1}{4\pi}\nabla\cdot[r\sin\theta B^*_{\phi,m\omega}\boldsymbol{B}_{{\rm pol},m\omega}], \tag{2}$$

where the asterisk denotes the complex conjugate. We define $\tau_{{\rm mag},m} \equiv \sum_\omega \tau_{{\rm mag},m\omega}$ and have

$$\sum_m \tau_{{\rm mag},m} = \sum_m\sum_\omega \tau_{{\rm mag},m\omega} = \tau_{\rm mag}. \tag{3}$$

The torque balance in the tachocline is shown in Figure 3(a), considered over about four dynamo cycles. Viscosity works to imprint the differential rotation from above by spinning up the equator and slowing down the mid-latitude regions, but is halted by the magnetic torque. The other torques that could play a role (Reynolds stress and meridional

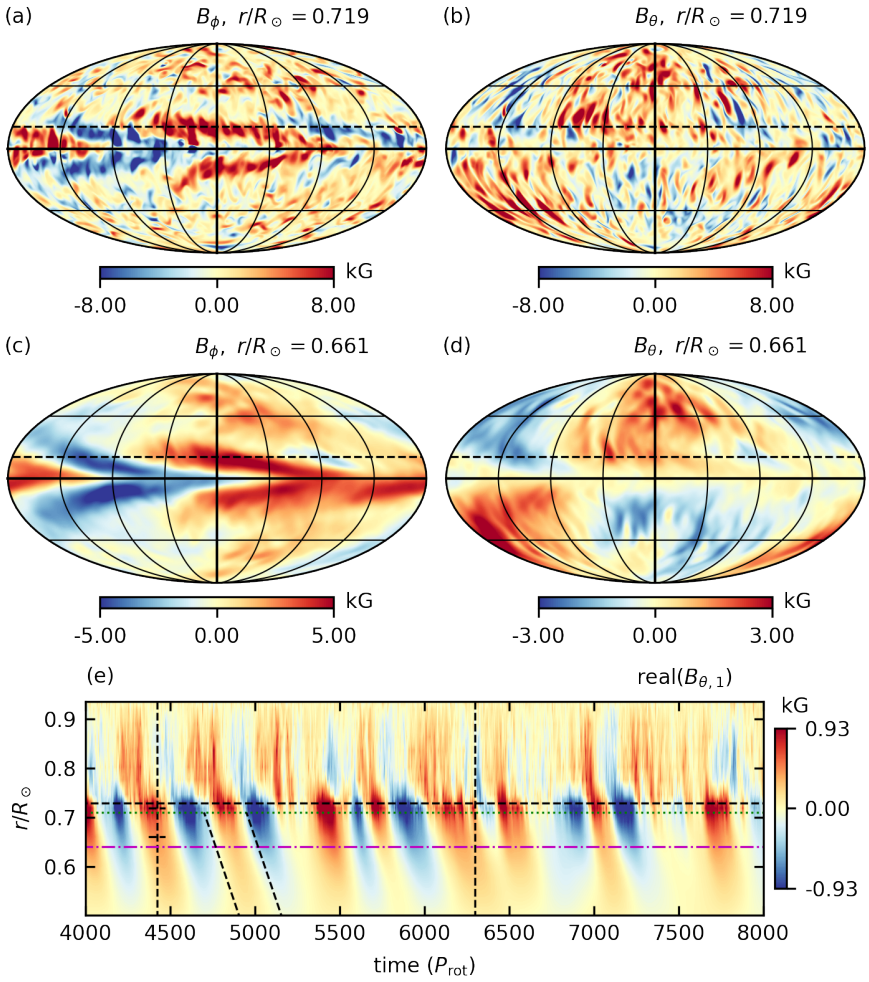

Figure 2. Non-axisymmetric, cycling dynamo. Snapshots of the horizontal magnetic fields at $t = 4422P_{\rm rot}$ for (a) B_ϕ in the overshoot layer, (b) B_θ in the overshoot layer, (c) B_ϕ in the tachocline, and (d) B_θ in the tachocline. Each field is plotted in full Mollweide view, latitudes and longitudes are marked every 45° by solid curves, and 15° latitude is marked by dashed line. (e) The real part of the $m = 1$ component of B_θ (see Equation (2)), plotted as a function of time and radius at 15° latitude. The vertical dashed lines denote the time interval considered in Figure 3. The two ticks on the leftmost vertical line show the depths sampled by the Mollweides. The diagonal dashed lines show the speed at which diffusion would imprint the oscillating field downward from the base of the overshoot layer according to the skin effect.

circulation) are negligible in the tachocline. The magnetic torque is almost entirely due to just the $m = 1$ and $m = 2$ components of the magnetic field, as shown by dotted blue curve in Figure 3(a). We consider the latitudinal variation of the frequency components $\tau_{{\rm mag},1\omega}$ in Figure 3(b) and $\tau_{{\rm mag},2\omega}$ in Figure 3(c). Remarkably, these profiles are all basically similar; each frequency component of the magnetic field separately opposes the viscous spread of the tachocline.

5. NON-AXISYMMETRIC FERRARO'S LAW

Ferraro's law of isorotation was originally stated for temporally steady and axi-symmetric magnetic fields in stellar radiative interiors: "Contours of isorotation tend to fall along poloidal magnetic field lines" (Ferraro 1937). The argument behind this law is perhaps even more relevant in the non-axisymmetric, cycling context. Differential rotation (nonzero $\nabla\Omega$) bends poloidal magnetic field lines to produce a toroidal field through mean shear. From the toroidal component of the MHD induction equation, we have

$$\frac{\partial B_\phi}{\partial t} \approx \underbrace{r\sin\theta \boldsymbol{B}_{\rm pol}\cdot\nabla\Omega}_{\text{mean shear}} \quad \underbrace{-\,v_r\frac{\partial B_\phi}{\partial r}}_{\text{toroidal pumping}} \quad \underbrace{-\,\{\nabla\times[\eta(r)\nabla\times\boldsymbol{B}]\}_\phi}_{\text{toroidal diffusion}} + \ldots \tag{4}$$

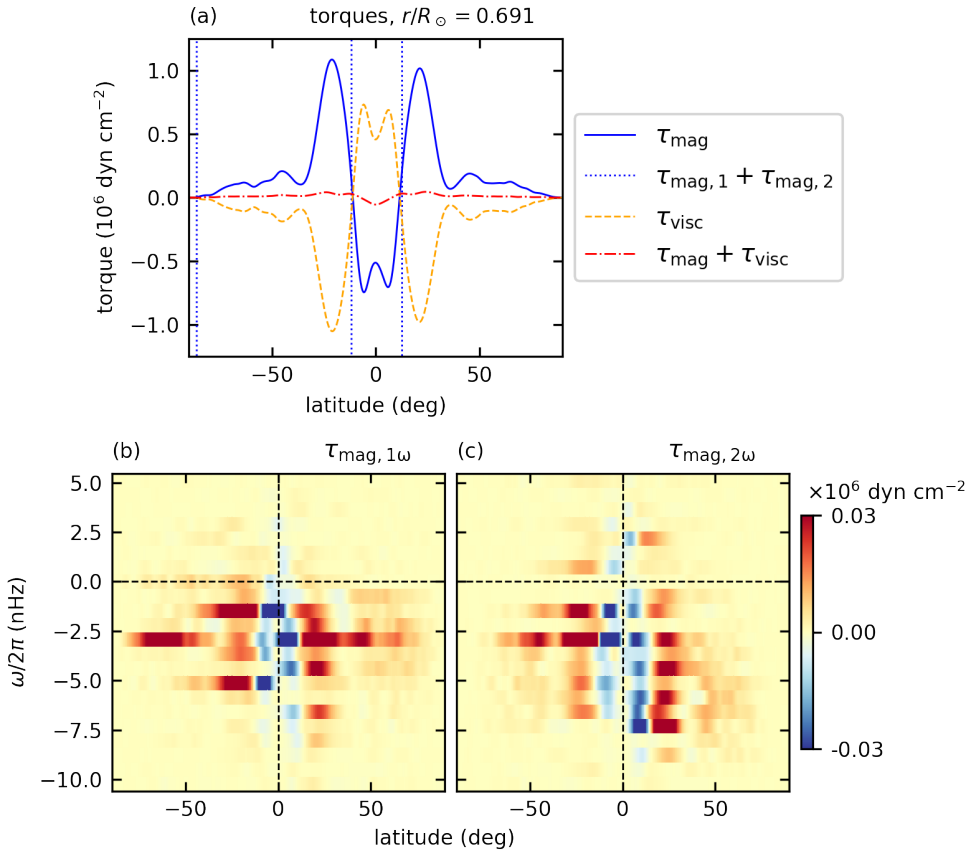

Figure 3. Magnetic torque maintaining the tachocline. We show torques averaged over the time interval $4422P_{\rm rot}$ to $6299P_{\rm rot}$, indicated by the dashed vertical lines in Figure 2(e). (a) The magnetic and viscous torques and their sum as functions of latitude in the tachocline. (b) and (c) The frequency-decomposed contributions to $\tau_{\rm mag,1}$ and $\tau_{\rm mag,2}$, respectively. The frequency resolution is 0.73 nHz and the Nyquist frequency is 5,000 nHz.

The ellipsis denote terms neglected from the full induction $[\nabla \times (\boldsymbol{v} \times \boldsymbol{B})]_\phi$, like compression and horizontal advection. Note that we define the induction by mean shear as the differential rotation (zonally and temporally averaged) bending the time-dependent, non-axisymmetric poloidal magnetic field. When the mean shear is dominant, Equation (4) yields $B_\phi \approx (r \sin\theta \boldsymbol{B}_{\rm pol} \cdot \nabla\Omega) t_{\rm bend}$, where $t_{\rm bend}$ is the timescale over which the shear $\nabla\Omega$ is imposed. From Equation (1), the associated torque due to magnetic tension is $\nabla \cdot \left[r^2 \sin^2\theta \left\langle \boldsymbol{B}_{\rm pol} (\boldsymbol{B}_{\rm pol} \cdot \nabla\Omega) t_{\rm bend} \right\rangle_{\rm t} \right]$, which tends to eliminate gradients in Ω parallel to $\boldsymbol{B}_{\rm pol}$. Assuming the magnetic torque dominates, equilibrium requires $\langle \boldsymbol{B}_{\rm pol} \cdot \nabla\Omega \rangle_{\rm t} = 0$. For an axisymmetric, temporally steady poloidal magnetic field, this reduces to the original Ferraro's law, $\langle \boldsymbol{B}_{\rm pol} \rangle_{\rm t} \cdot \nabla\Omega = 0$. However, as noted by Mestel & Weiss (1987), a non-axisymmetric or time-dependent field tends to yield solid-body rotation. For $\boldsymbol{B}_{\rm pol} \cdot \nabla\Omega$ to average to zero, the obvious solution is $\boldsymbol{B}_{\rm pol} \cdot \nabla\Omega = 0$ everywhere and at all times. If the direction of $\boldsymbol{B}_{\rm pol}$ varies, then we must have $\nabla\Omega = 0$.

6. MAGNETIZATION OF THE RADIATIVE INTERIOR

We consider the production of toroidal magnetic energy in Figure 4(a) ($\langle \cdots \rangle_{\rm sph}$ applied to the product of Equation (4) and $B_\phi/4\pi$). Note that the mean shear can be decomposed into its vertical ($r \sin\theta B_r \partial\Omega/\partial r$) and horizontal ($\sin\theta B_\theta \partial\Omega/\partial\theta$) components. In the radiative interior, strong toroidal field is sustained mostly by the horizontal mean shear (and to a lesser extent, by the vertical mean shear) and dissipated diffusively. Note that magnetic pumping (defined here to be magnetic energy production from radial advection) has a role in transporting B_ϕ from the convection zone to the base of the overshoot layer. The rapid radial oscillations in the pumping profile below the overshoot layer have negligible amplitude and are likely due to the many-celled meridional circulation in the stable region.

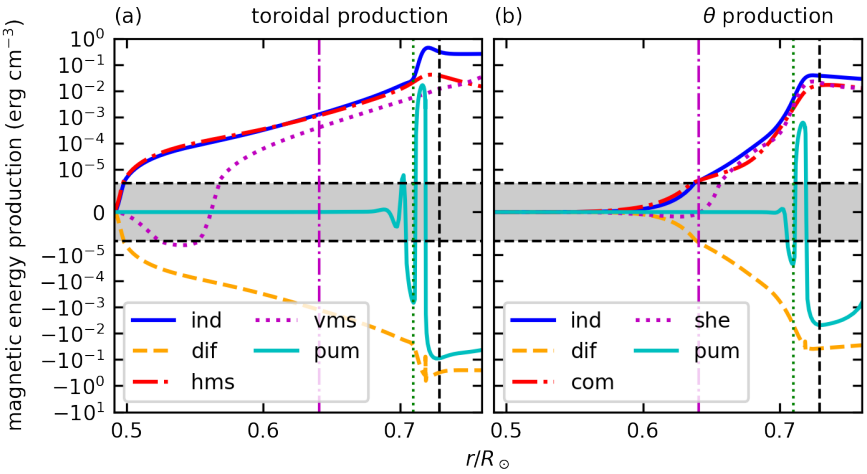

Figure 4. Dynamo action in the MHD case's radiative interior. Production of (a) $B_\phi^2/8\pi$ and (b) $B_\theta^2/8\pi$, plotted with respect to radius below $r/R_\odot = 0.760$. The terms labeled in Equations 4 and 5 are abbreviated as full induction (ind), diffusion (dif), horizontal mean shear (hms), vertical mean shear (vms), pumping (pum), compression (com), and shear (she). Each panel shares the same x- and y-axes. The y-axis is scaled logarithmically (unshaded region) for absolute values $> 3 \times 10^{-6}$ erg cm^{-3} and linearly (shaded region) otherwise.

Figure 4(a) shows that the MHD case's tachocline stems from strong B_θ, also consistent with Ferraro's law. Broadly speaking, B_θ in the radiative interior can arise either through inward diffusion of the convection zone's B_θ or through local inductive amplification. We have already seen from Figure 2(e) that the first of these mechanisms is significant. To isolate the second mechanism, we consider the θ-component of the induction equation:

$$\frac{\partial B_\theta}{\partial t} \approx \underbrace{-B_\theta \left(\frac{1}{r \sin\theta} \frac{\partial v_\phi}{\partial \phi} + \frac{\cot\theta}{r} v_\theta \right)}_{\theta \text{ compression}} + \underbrace{r(B_r \hat{\boldsymbol{e}}_r + B_\phi \hat{\boldsymbol{e}}_\phi) \cdot \nabla \left(\frac{v_\theta}{r} \right)}_{\theta \text{ shear}}$$
$$\underbrace{- v_r \frac{\partial B_\theta}{\partial r}}_{\theta \text{ pumping}} \underbrace{- \{\nabla \times [\eta(r) \nabla \times \boldsymbol{B}]\}_\theta}_{\theta \text{ diffusion}} + \ldots \tag{5}$$

As in Equation (4), the ellipsis denote terms neglected from the full induction $[\nabla \times (\boldsymbol{v} \times \boldsymbol{B})]_\theta$. The production of $B_\theta^2/4\pi$ ($\langle \cdots \rangle_{\text{sph}}$ applied to the product of Equation (5) and $B_\theta/4\pi$) is shown in Figure 4(b). On long timescales, B_θ is destroyed by diffusion and amplified inductively at all radii. The induction comes primarily from compression (the zonal squeezing of B_θ) and shear (the tilting of radial and toroidal field into B_θ). Like for B_ϕ, magnetic pumping deposits B_θ from the convection zone to the base of the overshoot layer.

7. DISCUSSION

Our MHD case represents a new type of fast MHD confinement scenario, in which the poloidal field penetrates downward diffusively, cycles quasi-periodically, is composed of non-axisymmetric partial wreaths, and is locally amplified in the deep layers by induction. The original fast MHD scenario relies on a turbulently enhanced magnetic diffusion to make the nominal solar-cycle skin depth (only ∼10 km) on par with the tachocline thickness (Forgács-Dajka & Petrovay 2001). However, the Sun's full dynamo field, which has modulations on many different timescales like grand minima and the biennial oscillation (e.g., Hathaway 2015), may extend deeper than this nominal skin depth. Any temporally steady component of the field, for example, would have spread far below the tachocline, even without turbulent diffusion (the molecular magnetic diffusion time across the radiative interior is ∼8 billion years; across the tachocline, ∼20 million years; see Brandenburg & Subramanian 2005). Because different frequency components of a dynamo can produce similar torques (Figure 3), the temporally steady field could work in concert with the cycling components to confine the solar tachocline.

We note that many prior global simulations with coupled convection zones and radiative interiors display strong horizontal velocities and magnetic fields below the overshoot layer, even when there is no explicit diffusivity (e.g.,

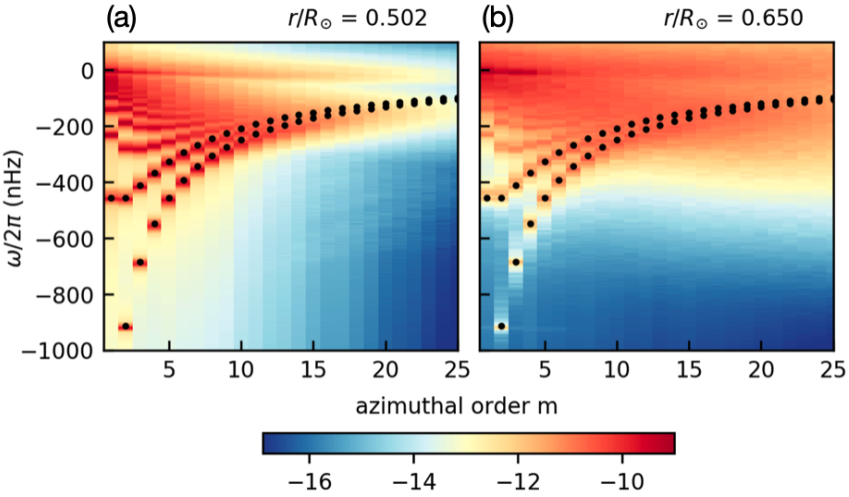

Figure 5. Rossby Waves in the radiative interior. Power in the radial vorticity (integrated over latitude) as a function of m and ω for (a) the deep interior and (b) the tachocline. For $\ell - m = 0$ and $\ell - m = 1$ (0 latitudinal nodes in the spherical harmonic and 1 node, respectively), the dispersion relation given by Equation (6) is plotted versus m using black dots. The power has been averaged over eight realizations of the wavefield, each of length $206 P_{\rm rot}$. For each realization, the frequency resolution is 5 nHz and the Nyquist frequency is 5,000 nHz.

Brun et al. 2011; Alvan et al. 2014; Guerrero et al. 2016; Bice & Toomre 2020, 2022). In Lawson et al. (2015), it is even suggested that local induction may be consistent with the achieved downward imprinting of magnetic field from a cycling Poynting flux.

If the poloidal field can be inductively amplified locally, then the precise value of the turbulent magnetic diffusion is even less relevant. A small seed poloidal field could grow to amplitudes capable of tachocline confinement. The source of strong horizontal motions has not previously been identified definitively, but may be a combination of shear, magnetic, and buoyancy instabilities (e.g., Dikpati & Gilman 1999; Gilman 2018). In our case, equatorial Rossby waves (Gizon et al. 2020) evince the clearest signature in the horizontal motions. Figure 5 shows the power in the radial vorticity with respect to m and ω (summed over all latitudes). We overlay the theoretical dispersion relation for equatorial Rossby waves,

$$\omega_{\ell m} = -\frac{2\Omega_0 m}{\ell(\ell+1)}, \tag{6}$$

where ℓ is the spherical-harmonic degree (e.g., Zaqarashvili et al. 2021). In the deep layers, the power in radial vorticity is closely aligned with Equation (6), with small frequency shifts due to the effects of the differential rotation and cycling magnetic field. There is also some significant low-m power at frequencies on the order of tens of nHz, which may in part be due to different $\ell - m$ ridges of Equation (6) converging to zero frequency for low m and high ℓ. Furthermore, Rossby waves in this frequency range would be significantly affected by the differential rotation and cycling dynamo, yielding critical-latitude, high-latitude, and MHD Rossby waves (Gizon et al. 2020; Zaqarashvili et al. 2021). In the tachocline, the Rossby waves lie amidst a largely featureless background, and their low-frequency signature is stronger. This background may be due to overshooting plumes, which should impart significant vorticity to the deeper layers in a stochastic fashion (Tobias et al. 1998).

In Gilman (1969), it was shown that Rossby waves in the convection zone could be baroclinically unstable and could achieve a complete dynamo loop (Zaqarashvili et al. 2021). Studies also shown that baroclinically unstable Rossby waves likely exist in the solar tachocline and could produce poloidal magnetic field (e.g., Charbonneau et al. 1999b; Gilman 2018; Zaqarashvili et al. 2021). Many of these instabilities set in at $m = 1$ and $m = 2$ (e.g., Garaud 2001; Lawson et al. 2015; Gilman 2018). In Charbonneau et al. (1999b), the shear instability arise from critical-latitude Rossby waves, which appear when the frequency from Equation (6) is comparable to the latitudinal differential rotation contrast. These results are strongly suggestive of critical-latitude (potentially unstable) Rossby waves forming the low-frequency signature of power in Figure 5.

Equatorial and critical-latitude Rossby waves have been identified helioseismically (Löptien et al. 2018; Gizon et al. 2020). The critical-latitude modes, in particular, may have most of their energy near the base of the convection zone (Gizon et al. 2021). They could thus produce strong horizontal motions at least down into the tachocline and our work suggests that such motions may extend even deeper. In summary, we offer two new perspectives on the solar interior. First, tachocline confinement is possible by a self-excited, 3-D dynamo magnetic field that is non-axisymmetric and has multiple cycling frequency components. Second, strong horizontal motions may amplify magnetic field locally through induction, even below the overshoot layer. Both perspectives suggest a dynamically active radiative interior and challenge its perceived role as a quiescent storage reservoir.

We thank M. Miesch, N. Brummell, and P. Garaud for helpful discussions. L. Matilsky was primarily supported during this work by the Future Investigators in NASA Earth and Space Sciences Technology (FINESST) award 80NSSC19K1428. C. Blume was supported by a University of Colorado George Ellery Hale Graduate Fellowship. This research was also supported by NASA Heliophysics through grants NNX13AG18G, NNX17AG22G, 80NSSC18K1127, 80NSSC17K0008, 80NSSC18K1125, 80NSSC19K0267, and 80NSSC20K0193. Computational resources were provided by the NASA High-End Computing (HEC) Program through the NASA Advanced Supercomputing (NAS) Division at Ames Research Center. Rayleigh is hosted and receives support from the Computational Infrastructure for Geodynamics (CIG), which is supported by the National Science Foundation awards NSF-0949446 and NSF-1550901. Input files and checkpoint snapshots for the HD and MHD cases will be hosted on the publicly accessible Rayleigh Simulation Library (https://osf.io/j275z/), with more extensive datasets available from the authors upon request.

APPENDIX

A. BACKGROUND THERMODYNAMIC STATE

In our models, we employ a spherically symmetric, time-independent background state that represents the stable-to-unstable transition in the Sun that occurs at the base of the convection zone. We choose a simplified entropy-gradient profile $d\overline{S}/dr$, which is zero in the convection zone, has a constant positive value in the stable layer, and has smooth matching in between:

$$\frac{d\overline{S}}{dr} = \begin{cases} \sigma & r \leq r_0 - \delta \\ \sigma\left\{1 - \left[1 - \left(\frac{r-r_0}{\delta}\right)^2\right]^2\right\} & r_0 - \delta < r < r_0 \\ 0 & r \geq r_0, \end{cases} \tag{A1}$$

where $\sigma \equiv 10^{-2}$ erg g^{-1} K^{-1} cm^{-1} and $\delta \equiv 0.05 R_\odot$. We choose a background gravitational-acceleration profile of

$$g(r) = \frac{GM_\odot}{r^2}, \tag{A2}$$

where $G = 6.67 \times 10^{-8}$ dyn cm^2 g^{-2} is the gravitational constant and $M_\odot = 1.99 \times 10^{33}$ g is the mass of the Sun. We write the pressure, density, and temperature as $\overline{P}(r)$, $\overline{\rho}(r)$, and $\overline{T}(r)$, respectively. Hydrostatic balance and the ideal-gas condition yields

$$\overline{T}(r) = -\exp\left[\frac{\overline{S}(r)}{c_\mathrm{p}}\right]\int_{r_0}^{r}\frac{g(x)}{c_\mathrm{p}}\exp\left[-\frac{\overline{S}(x)}{c_\mathrm{p}}\right]dx + \overline{T}_0\exp\left[\frac{\overline{S}(r)}{c_\mathrm{p}}\right], \tag{A3a}$$

$$\overline{P}(r) = \overline{\rho}_0\mathcal{R}\overline{T}_0\exp\left[-\frac{\overline{S}(r)}{\mathcal{R}}\right]\left[\frac{\overline{T}(r)}{T_0}\right]^{\gamma/(\gamma-1)}, \tag{A3b}$$

$$\text{and} \qquad \overline{\rho}(r) = \overline{\rho}_0\exp\left[-\frac{\overline{S}(r)}{\mathcal{R}}\right]\left[\frac{\overline{T}(r)}{T_0}\right]^{1/(\gamma-1)}. \tag{A3c}$$

Here, $c_\mathrm{p} = 3.50 \times 10^8$ erg g^{-1} K^{-1} is the specific heat at constant pressure, $\gamma = 1.67$ is the ratio of specific heats, and $\mathcal{R} = (\gamma - 1)c_\mathrm{p}/\gamma$ is the gas constant. We choose $\overline{\rho}_0 = 0.181$ g cm^{-3} and $\overline{T}_0 = 2.11 \times 10^6$ K, consistent with solar models (Christensen-Dalsgaard et al. 1996), and $\overline{S}(r_0) = 0$. We choose the internal heating profile $Q(r)$ to occupy the convection zone only:

$$Q(r) = \alpha \tanh\left[\frac{r - r_0}{\delta_\mathrm{heat}}\right][\overline{P}(r) - \overline{P}(r_\mathrm{max})], \tag{A4}$$

where $\delta_\mathrm{heat} = 0.03 R_\odot$ and the constant α is chosen so the volume integral of $Q(r)$ over the whole shell is the solar luminosity. In the convection zone, the reference state is nearly identical to our prior work and closely resembles the standard solar "model S" (Featherstone & Hindman 2016; Matilsky et al. 2020; Hindman et al. 2020).

In keeping with past work (Brun et al. 2017), we define the convection zone (and hence its base r_bcz) to be the region in which the convective heat flux (or enthalpy flux F_e) is positive. Similarly, we define the base of the overshoot layer r_ov as the location below which F_e is negative but very close to zero (we choose a tolerance of 5% the minimum value of F_e in the overshoot layer). Though the nominal transition between stability and instability occurs at r_0, convective heat transport moves the base of the convection zone slightly upward to $r_\mathrm{bcz} > r_0$. Convective downflows overshoot into a thin layer within the stable region. The base of this overshoot layer (defined to be the location below which there is negligible vertical transport of heat by the fluid flow—and concurrently very little radial velocity) is located at $r_\mathrm{ov} < r_0$. For the MHD case, $r_\mathrm{bcz} = 0.729 R_\odot$ and $r_\mathrm{ov} = 0.710 R_\odot$. For the HD case, $r_\mathrm{bcz} = 0.726 R_\odot$ and $r_\mathrm{ov} = 0.701 R_\odot$.

B. NON-DIMENSIONAL PARAMETERS

The parameter regime of our simulations is described by four non-dimensional numbers (five for the MHD case) (Hindman et al. 2020): the flux Rayleigh number $\mathrm{Ra_F}$, the Ekman number Ek, the dissipation number Di, the thermal Prandtl number Pr, and (for the MHD case only) the magnetic Prandtl number $\mathrm{Pr_m}$. The first four numbers are the same in both simulations. These numbers are defined and evaluated as

$$\begin{aligned}
\mathrm{Ra_F} &\equiv \frac{\tilde{g}\tilde{F}H^4}{c_\mathrm{p}\tilde{\rho}\tilde{T}\tilde{\nu}\tilde{\kappa}^2} = 7.50 \times 10^5, \\
\mathrm{Ek} &\equiv \frac{\tilde{\nu}}{\Omega_0 H} = 1.07 \times 10^{-3}, \\
\mathrm{Di} &\equiv \frac{\tilde{g}H}{c_\mathrm{p}\tilde{T}} = 1.72, \\
\mathrm{Pr} &\equiv \frac{\tilde{\nu}}{\tilde{\kappa}} = 1, \\
\text{and} \quad \mathrm{Pr_m} &\equiv \frac{\tilde{\nu}}{\tilde{\eta}} = 4.
\end{aligned}$$

Here, we define the system's length-scale as $H \equiv r_\mathrm{max} - r_0$, the tildes denote volume averages of the underlying reference-state radial profiles (from r_0 to r_max), and $F(r) \equiv (1/r^2)\int_{r_\mathrm{min}}^{r} Q(x)x^2 dx$ is approximately the energy that convection and conduction must carry to maintain a statistically steady state.

In each simulation's equilibrated state, several diagnostic non-dimensional numbers describe the system: the Reynolds number Re, the magnetic Reynolds number $\mathrm{Re_m}$, the Rossby number Ro, and the buoyancy parameter B. These are defined as

$$\begin{aligned}
\mathrm{Re} &\equiv \frac{\tilde{v}'H}{\tilde{\nu}}, \\
\mathrm{Re_m} &\equiv \frac{\tilde{v}'H}{\tilde{\eta}}, \\
\mathrm{Ro} &\equiv \frac{\tilde{v}'}{2\Omega_0 H}, \\
\text{and} \quad \mathrm{B} &\equiv \frac{\widetilde{N^2}}{\Omega_0^2}
\end{aligned}$$

Table B1. Diagnostic non-dimensional numbers for the HD and MHD cases. Diagnostic parameters defined in the text are shown volume-averaged over the convection zone, overshoot layer, and radiative interior.

	HD case			MHD case		
	Convection zone	Overshoot layer	Radiative interior	Convection zone	Overshoot layer	Radiative interior
Re	45.8	58.4	15.7	36.3	21.6	2.86
$\mathrm{Re_m}$	-	-	-	145	86.3	11.5
Ro	2.47×10^{-2}	1.48×10^{-2}	2.59×10^{-3}	1.96×10^{-2}	5.58×10^{-3}	4.84×10^{-4}
B	-0.725	1,130	28,000	-0.710	206	26,700

and evaluated in Table B1. Here, the tildes denote combined temporal and volume averages, $v' \equiv |\boldsymbol{v}'|$, $N^2 \equiv (g/c_\mathrm{p})[d\overline{S}/dr + \langle dS'/dr \rangle_\mathrm{sph}]$ is the squared buoyancy frequency, and S' is the entropy fluctuation from the background state.

REFERENCES

Acevedo-Arreguin, L. A., Garaud, P., & Wood, T. S. 2013, MNRAS, 434, 720, doi: 10.1093/mnras/stt1065

Alvan, L., Brun, A. S., & Mathis, S. 2014, A&A, 565, A42, doi: 10.1051/0004-6361/201323253

Anders, E. H., Vasil, G. M., Brown, B. P., & Korre, L. 2020, PhRevF, 5, doi: 10.1103/physrevfluids.5.083501

Barnabé, R., Strugarek, A., Charbonneau, P., Brun, A. S., & Zahn, J.-P. 2017, A&A, 601, A47, doi: 10.1051/0004-6361/201630178

Bice, C. P., & Toomre, J. 2020, ApJ, 893, 107, doi: 10.3847/1538-4357/ab8190

—. 2022, ApJ, in press

Brandenburg, A., & Subramanian, K. 2005, PhRep, 417, 1, doi: 10.1016/j.physrep.2005.06.005

Brown, T. M., Christensen-Dalsgaard, J., Dziembowski, W. A., et al. 1989, ApJ, 343, 526, doi: 10.1086/167727

Brun, A. S., Miesch, M. S., & Toomre, J. 2011, ApJ, 742, 79, doi: 10.1088/0004-637x/742/2/79

Brun, A. S., Strugarek, A., Varela, J., et al. 2017, ApJ, 836, 192, doi: 10.3847/1538-4357/aa5c40

Charbonneau, P., Christensen-Dalsgaard, J., Henning, R., et al. 1999a, ApJ, 527, 445, doi: 10.1086/308050

Charbonneau, P., Dikpati, M., & Gilman, P. A. 1999b, ApJ, 526, 523, doi: 10.1086/307989

Charbonneau, P., & MacGregor, K. B. 1997, ApJ, 486, 502, doi: 10.1086/304485

Christensen-Dalsgaard, J., Däppen, W., Ajukov, S. V., et al. 1996, Sci., 272, 1286, doi: 10.1126/science.272.5266.1286

Dikpati, M., & Gilman, P. A. 1999, ApJ, 512, 417, doi: 10.1086/306748

Featherstone, N. A., Edelmann, P. V. F., Gassmoeller, R., et al. 2021, Rayleigh 1.0.1, doi: http://doi.org/10.5281/zenodo.5774039

Featherstone, N. A., & Hindman, B. W. 2016, ApJ, 818, 32, doi: 10.3847/0004-637x/818/1/32

Ferraro, V. C. A. 1937, MNRAS, 97, 458, doi: 10.1093/mnras/97.6.458

Ferriz-Mas, A., & Schuessler, M. 1994, ApJ, 433, 852, doi: 10.1086/174694

Forgács-Dajka, E., & Petrovay, K. 2001, SoPh, 203, 195, doi: 10.1023/a:1013389631585

Garaud, P. 2001, MNRAS, 324, 68, doi: 10.1046/j.1365-8711.2001.04245.x

—. 2002, MNRAS, 329, 1, doi: 10.1046/j.1365-8711.2002.04961.x

—. 2020, ApJ, 901, 146, doi: 10.3847/1538-4357/ab9c99

Gilman, P., & Dikpati, M. 2014, ApJ, 787, 60, doi: 10.1088/0004-637x/787/1/60

Gilman, P. A. 1969, J. Atm. Sci., 26, 1003, doi: 10.1175/1520-0469(1969)026⟨1003:baarwi⟩2.0.co;2

—. 2018, ApJ, 853, 65, doi: 10.3847/1538-4357/aaa4f4

Gilman, P. A., & Glatzmaier, G. A. 1981, ApJS, 45, 335, doi: 10.1086/190714

Gizon, L., Fournier, D., & Albekioni, M. 2020, A&A, 642, A178, doi: 10.1051/0004-6361/202038525

Gizon, L., Cameron, R. H., Bekki, Y., et al. 2021, A&A, 652, L6, doi: 10.1051/0004-6361/202141462

Gough, D. O., & McIntyre, M. E. 1998, Nat., 394, 755, doi: 10.1038/29472

Guerrero, G., Smolarkiewicz, P. K., de Gouveia Dal Pino, E. M., Kosovichev, A. G., & Mansour, N. N. 2016, ApJ, 819, 104, doi: 10.3847/0004-637x/819/2/104

Hathaway, D. H. 2015, LRSP, 7, doi: 10.12942/lrsp-2010-1

Hindman, B. W., Featherstone, N. A., & Julien, K. 2020, ApJ, 898, 120, doi: 10.3847/1538-4357/ab9ec2

Howe, R. 2009, Living Review of Solar Physics, 6, doi: 10.12942/lrsp-2009-1

Howe, R., Christensen-Dalsgaard, J., Hill, F., et al. 2000, Sci., 287, 2456, doi: 10.1126/science.287.5462.2456

Lawson, N., Strugarek, A., & Charbonneau, P. 2015, ApJ, 813, 95, doi: 10.1088/0004-637x/813/2/95

Löptien, B., Gizon, L., Birch, A. C., et al. 2018, Nat. Astron., 2, 568, doi: 10.1038/s41550-018-0460-x

Matilsky, L. I., Hindman, B. W., & Toomre, J. 2020, ApJ, 898, 111, doi: 10.3847/1538-4357/ab9ca0

Matilsky, L. I., & Toomre, J. 2020a, ApJ, 892, 106, doi: 10.3847/1538-4357/ab791c

—. 2020b, in Astrophysics and Space Science Proceedings (Springer International Publishing), 197–199, doi: 10.1007/978-3-030-55336-4_27

Matilsky, L. I., & Toomre, J. 2021, in 20.5th Cambridge Workshop on Cool Stars, Stellar Systems, and the Sun, ed. S. J. Wolk (Zenodo), doi: 10.5281/ZENODO.4750777

Matsui, H., Heien, E., Aubert, J., et al. 2016, Geochem., Geophys., Geosys., 17, 1586, doi: 10.1002/2015gc006159

Mestel, L., & Weiss, N. O. 1987, MNRAS, 226, 123, doi: 10.1093/mnras/226.1.123

O'Mara, B., Miesch, M. S., Featherstone, N. A., & Augustson, K. C. 2016, Adv. Space Res., 58, 1475, doi: 10.1016/j.asr.2016.03.038

Parker, E. N. 1993, ApJ, 408, 707, doi: 10.1086/172631

Spiegel, E. A., & Zahn, J.-P. 1992, A&A, 265, 106

Spruit, H. C., & van Ballegooijen, A. A. 1982, A&A, 106, 58

Tobias, S. M., Brummell, N. H., Clune, T. L., & Toomre, J. 1998, ApJ, 502, L177, doi: 10.1086/311501

Wood, T. S., & Brummell, N. H. 2012, ApJ, 755, 99, doi: 10.1088/0004-637x/755/2/99

—. 2018, ApJ, 853, 97, doi: 10.3847/1538-4357/aaa6d5

Zaqarashvili, T. V., Albekioni, M., Ballester, J. L., et al. 2021, SpSciRev, 217, doi: 10.1007/s11214-021-00790-2